Implementing 3D Digital Image Correlation to Study the Dynamics of Globally-Coupled Multistable Structures

Undergraduate Honors Thesis

Presented in Partial Fulfillment of the Requirements for Graduation with
Honors Research Distinction in the Department of Mechanical and Aerospace Engineering
of The Ohio State University

By

Adam DeNise

Undergraduate Program in Mechanical Engineering

The Ohio State University

April 2019

Thesis Committee:

Ryan L. Harne, Advisor

Manoj Srinivasan

Copyright by

Adam DeNise

2019

ABSTRACT

Modern structural systems that employ slender structures to minimize cost and weight may undergo nonlinear dynamics that can be harmful to long-term structural integrity. For example, slender aerostructures employed for future hypersonic aircraft may experience detrimental dynamic behaviors due to combined loads of hypersonic flight. Skin buckling is a result of the combined loads and leads to wear on structural components, and failure. The skin buckling is evidence of multistability, a condition analogous to an array of coupled, bistable beams, that each contain two stable equilibrium configurations. While the influences of local coupling between adjacent bistable beams on the system dynamic behaviors has previously been assessed, the more expansive global coupling mechanisms have not been investigated. Global coupling influences are those that provide direct connection between one bistable component and a non-nearest neighbor by way of interfaces that are shared throughout the system. This research seeks to establish an experimental approach to uncover first insights on global coupling mechanisms that influence the resulting dynamic behaviors of multistable structures. An array of cantilevered beams that share a common overhang boundary is fabricated to allow control over a simplified form of global coupling. Once fabricated, the system is configured with attractive magnets near the end of the beams to induce bistable states and thus a multistable structure. A new experimental infrastructure based on the three-dimensional digital image correlation (3D DIC) method is implemented to provide full-field motion mapping of the system displacements. Then, experiments investigate how global coupling parameters influence the dynamic behavior of the beam system when subjected to harmonic mechanical loads. The results of this research will guide development of future investigations to analyze the influences of global coupling in multistable structures in a complementary theoretical framework.

ACKNOWLEDGMENTS

First, I would like to thank my advisor, Prof. Ryan L. Harne, for his constant guidance and support. This research would not be successful without him.

I also am thankful for Prof. Srinivasan for his help as my committee member.

Finally, I would like to acknowledge support from the OSU College of Engineering for the Undergraduate Honors Research Scholarship.

All experiments presented in this research were conducted in the Laboratory of Sound & Vibration Research (LSVR), which is directed by Prof. Harne.

TABLE OF CONTENTS

LIST OF FIGURES

LIST OF TABLES

1 INTRODUCTION

1.1 Motivation

Hypersonic aircraft are of significant domestic and international interest. Hypersonic flight occurs at rates more than 5 times the speed of sound (Mach 5) whereas modern commercial airliners cruise around Mach 0.7. A difficult obstacle to overcome in the development of hypersonic aircraft is the combination of loads caused by the extreme operating conditions [1]. These aircraft employ thin and slender skin panels on the wings, control surfaces, and fuselages. If a skin panel is designed only for aerodynamic purposes, the combined loads will determine the dimensions and geometries of the panel [1]. To meet the performance requirements of hypersonic aircraft, skin panels must be lightweight and slender to maximize fuel efficiency and other performance standards. Yet, this conflicts with the strength demands needed to withstand the aerodynamic, thermal, and acoustic loads [2] [3]. Consequently, the lightweight, slender structures may undergo severe nonlinear dynamic behaviors during operation, such as flutter, buckling, and snap-through. The buckling of aircraft panels is termed skin buckling, which is evidence of multistability. The skin panels undergo an alteration of their surface into multiple, stable equilibria. Skin buckling is observed on the SR-71 Blackbird [4] [5], a research hypersonic aircraft developed by Lockheed Martin, in Figure 1(a). Closer to the speeds of commercial airliners, skin buckling has also been revealed on the Boeing B-52 [6], seen in Figure 1(b).

Figure 1: Skin buckling on aircraft, from [4]. (a) SR-71 Blackbird; (b) Boeing B-52.

If a mechanical system is multistable, the system will experience multiple stable equilibrium configurations [7]. The simplest case of multistability is bistability, in which a system contains two statically stable equilibria, between which lies an unstable equilibrium. To advance from one statically stable equilibrium to another, a structure must exhibit an interwell response, a nonlinear dynamic behavior associated with large oscillations between stable equilibria [8]. Another term for interwell is *snap-through*, an undesirable response for structural applications. In addition to large oscillations between stable equilibria, smaller oscillations may occur around one stable equilibrium, which is termed an intrawell response. To illustrate this phenomenon, an example of the potential energy relationship with displacement of a bistable structure is shown in Figure 2. The blue and green circles represent the stable equilibria, where a local potential

energy well exists. Snap-through occurs when the energy of the system exceeds the barrier presented by the unstable equilibrium, shown by a red circle. Intrawell occurs when energy of the system is not enough to exceed the barrier, resulting in oscillations about a stable equilibrium.

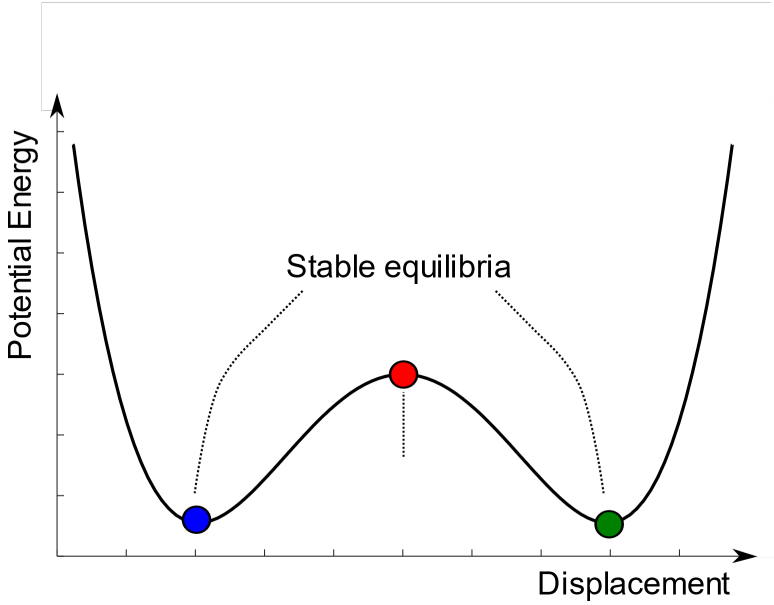

Figure 2: Potential energy-displacement relationship of a bistable system.

1.2 State-of-the-Art

The dynamic responses of bistable beams have been investigated by researchers under harmonic and stochastic excitation parameters. General multistable structural systems, comprised of bistable constituents, contain complex dynamic behaviors, making it challenging to elucidate the underlying phenomena. Indeed, bistable structures also exhibit complex dynamics. Yet, utilizing the archetypal nature of a bistable beam, when compared to a multistable structure composed of many bistable constituents, allow for researchers to focus on developing theoretical and computational methods. To uncover excitation parameters that lead to snap-through of a multi-degree-of-freedom (DOF) curved panel, Wiebe et al. [9] studied the excitations that lead to snap-through dynamics for a single degree of freedom (SDOF) oscillator with Duffing-type potential wells.

The many skin panels on an aircraft, connected through stiffening components, suggest that the overall dynamic response of one panel is influenced by those of its neighbors [10]. Indeed, Harne and Goodpaster [4] utilized analysis and experimental techniques to investigate the local coupling influences of multistable structures subjected to harmonic mechanical loads, demonstrating the importance of such nearest neighbor influences. In addition, strong coupling has been revealed among the dynamics of neighboring stiffened panels at the onset of buckling [11]. These examples demonstrate that local coupling is highly influential on the overall dynamic response and the fatigue life for nearest neighboring multistable structures. Yet, an understanding on the roles of global coupling has yet to be uncovered. Global coupling provides a direction connection between one bistable component and a non-nearest neighbor by way of interfaces, such as

shared boundaries. To exemplify global coupling, consider the system from [4] where mass-spring-damper sub-systems are assembled in a chain, in Figure 3. Springs K_{12} and K_{23} provide local coupling between nearest neighbors. Spring K_{13} provides coupling between non-nearest neighbors, which may be emblematic of general boundary interactions between hypersonic aircraft panels.

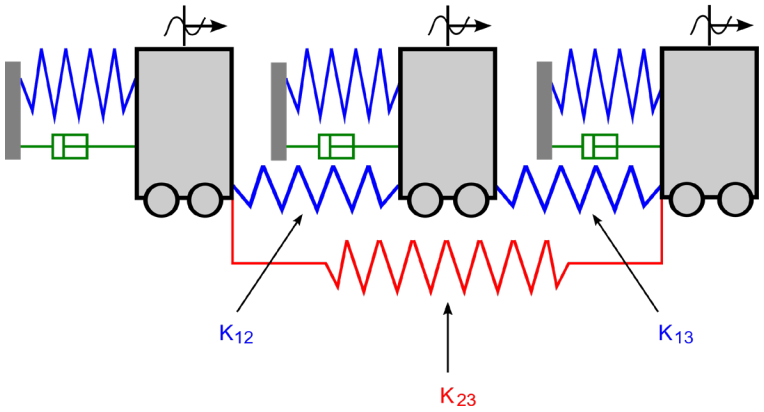

Figure 3: Beams treated as mass-spring-damper systems. Local coupling between nearest neighbors corresponding to springs K12 and K23. Global coupling between non-nearest neighbors corresponding to spring K13.

In fact, global coupling has been studied on the micromechanical scale for chemical mass detection and mode localization with cantilever beam oscillators [12] [13] [14] [15]. To vary the influence of the global coupling, the parameters of the shared boundary that supports the microcantilevers, termed the overhang, was adjusted [16]. These geometries are advantageous for investigating the roles of global coupling on the dynamics of multistable structures.

Furthermore, directly studying multistable structures is a challenge. Researchers currently employ finite element (FE) models, numerical simulations, and reduced order methods to study these structures. Yet, verification methods of analytical models have proved to be computationally expensive. To combat this, Goodpaster et al. [17] implemented an expanded analytical framework from [4] along with an enhanced initial guess algorithm to investigate the modal response and nonlinear coupling exhibited by multistable structures. Researchers have also shown that reduced order models can decrease the cost of simulation models [18]. Due to the multiphysics environment of hypersonic flight, researchers have expanded these models to characterize the impedance of thermomechanically coupled structures [19] and investigate the fluid-thermal-structural interactions of panels that are thermally buckled and subjected to random acoustic loads [20]. At the same time, new experimental methods such as 3D digital image correlation (DIC) are emerging as a valuable tool for investigation [21]. With the ability to provide full-field motion mapping, 3D DIC can experimentally verify the accuracy of FE models, which have been questioned for their accuracy nearing points of instability [8]. These advanced methods are providing new means to investigate and verify the nonlinear dynamics of multistable structures.

1.3 Research Goal

The goal of this research is to establish 3D DIC as an experimental infrastructure to experimentally investigate the influences of global coupling on the nonlinear dynamics of multistable structures subjected to harmonic excitations. The underlying mechanisms of energy transfer and exchange will be studied using this emerging experimental approach of 3D DIC. To achieve this goal, an archetypal multistable structural system consisting bistable, cantilevered beams with controllable global coupling elements is designed and fabricated. Next, experiments are conducted to investigate the influences of global coupling parameters on the dynamic response of the beams when subjected to harmonic mechanical loads.

1.4 Overview of Thesis

The organization of this thesis is as follows. Chapter 2 describes the experimental setup of the archetypal multistable structure in terms of fabrication and preparation for digital image correlation. It also describes the data acquisition equipment and types of testing methods. Chapter 3 presents the experimental results, including a discussion on the observed impact of global coupling on the dynamic response. Chapter 4 summarizes these methods and observations and recommends potential direction for future studies.

2 EXPERIMENTAL METHODS

2.1 Design and Fabrication of Archetypal Multistable Structure

To measure the dynamic response of bistable structures, it is common to use an experimental platform that includes an axially compressed beam that is post-buckled [8] [22]. These platforms are advantageous to induce buckling in the fundamental mode. Yet, this research aims to explore methods to study globally-coupled beams. Therefore, utilizing structural geometries inspired from micromechanical studies [16], along with magnetoelastic techniques to introduce nonlinearities by attractive magnets acting on a ferromagnetic beam tip [23], enables one to investigate a multistable, globally coupled beam system. The structure that is designed and fabricated for this research is shown in Figure 4. The beams are referred to as beams 1, 2, and 3, as shown in the image. The acrylic beams are machined using a laser cutter. The shared boundary, termed the overhang, between the beams allows for the beams to be globally coupled together. The extent of this global coupling is controllable by adjusting the cantilevered length of the overhang. Steel extensions are used to interact with permanent neodymium magnets, as seen in Figure 4(b) and Figure 5. The magnets provide attractive forces that oppose the direction of linear elastic forces [24], allowing for a controllable extent of bistability. Base excitations are provided by mounting the structural system to an electrodynamic shaker table.

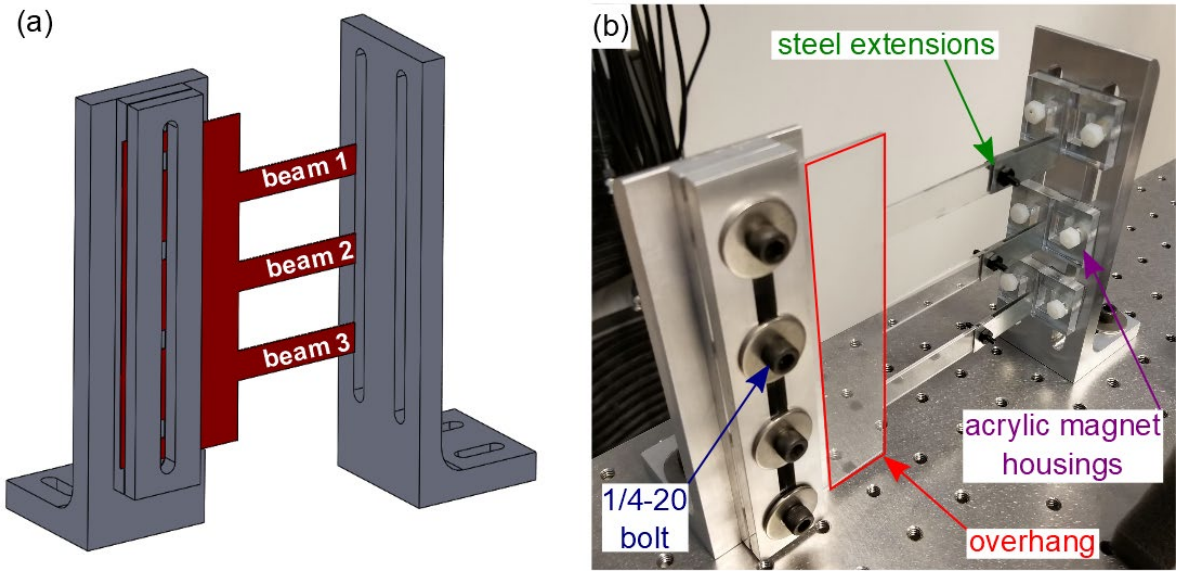

Figure 4: Globally-coupled multistable structural system. (a) SOLIDWORKS design; (b) experimental architecture

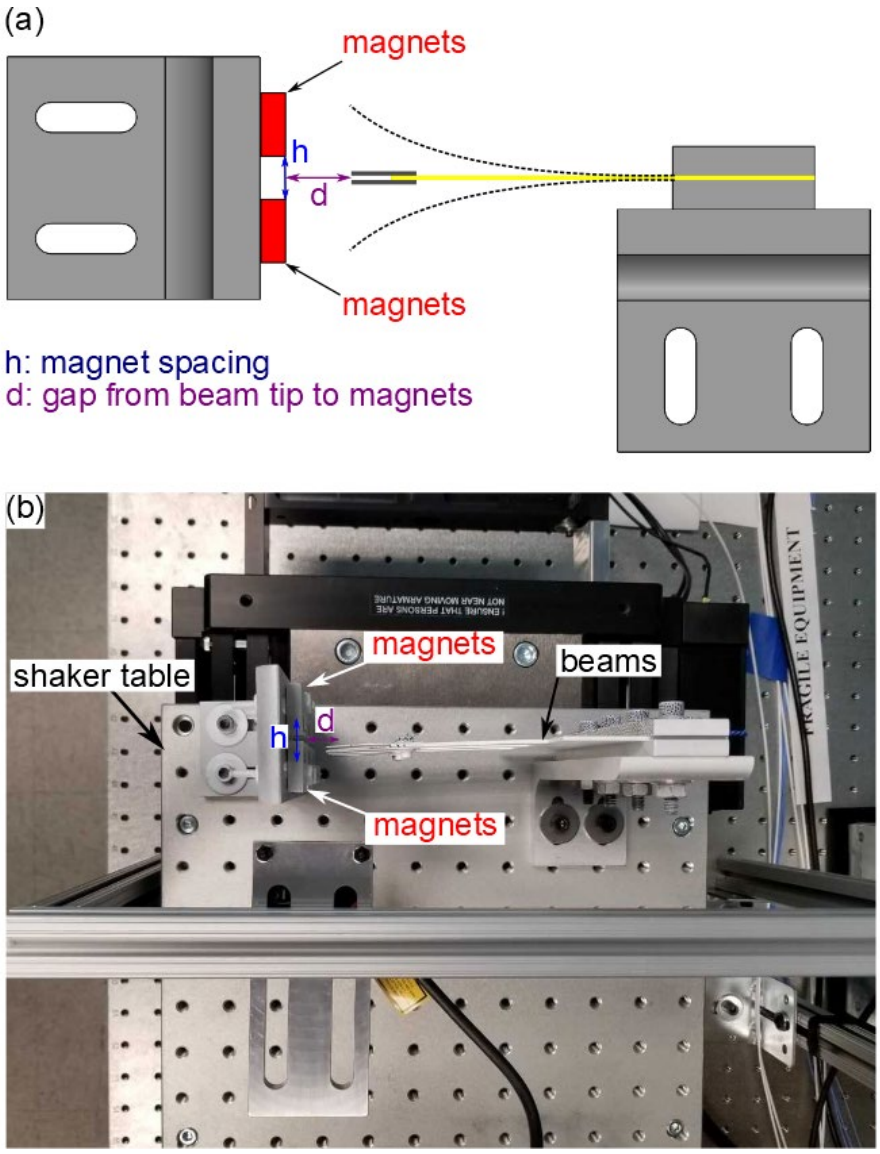

Figure 5: Top view of globally-coupled multistable structural system. (a) SOLIDWORKS design with labels; (b) experimental architecture mounted on shaker table

Overall, this experimental system is a simplified representation of the complicated skin buckling on aircraft panels. Although the beams in this system are not buckled in the sense of axial compression, they are bistable due to the attraction to the permanent magnets. The beams are long compared to their thickness, as are skin panels. In this sense, the bistable beams imitate the challenges that skin panels face when panel modes are buckled due to a combination of aerodynamic, thermal, and acoustic loads. The overhang is similar to the rib-stiffeners and rivets, components that break up continuous aircraft panels while forming shared boundaries between such panels.

2.2 Preparation for 3D DIC Analysis

Digital Image Correlation requires the test specimens to be carefully prepared. For accurate correlation, consistent speckle patterns, high contrast images, and diffuse lighting are a few important factors playing a major role in the results. A speckle pattern along with calibration techniques are required.

2.2.1 Application of speckle pattern

To measure the full-field displacements of the beams, a speckle pattern is applied to the surface of the structure. First each component was separately spray painted matte white (Krylon FUSION ALL-IN-ONE Matte White). Then the speckle pattern was applied using a fine-point Sharpie marker. This allowed for excellent control over the size of each dot, spacing between dots, and flexibility over complex geometry. The speckle pattern needs to be random in order that the numerous subsets of the pattern can be tracked and correlated throughout the motion. The pattern needs to be evenly distributed between black dots and white paint. The dots in the speckle pattern are recommended to be 3-5 pixels in size [25]. The results of this pattern are seen in Figure 6.

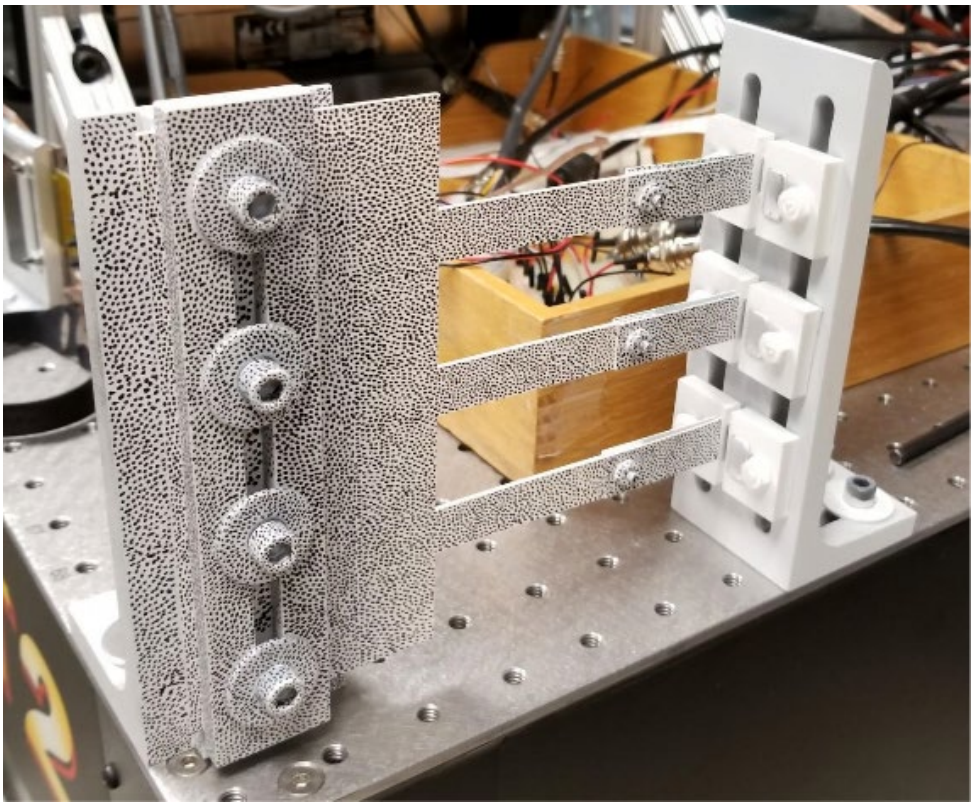

Figure 6: Speckle pattern applied to surface of experimental architecture

2.2.2 Camera calibration

2D DIC does not always require calibration, depending on the lens distortion [21]. Yet, 3D DIC needs calibration to ultimately establish a 3D world-coordinate system, while calculating intrinsic parameters of the cameras and using triangulation to compute the extrinsic parameters as well. This research utilizes MultiDIC, an open-source MATLAB toolbox which utilizes Ncorr for 2D DIC and reconstructs 3D surfaces

from stereo-pairs of cameras to obtain 3D displacements [26]. For MultiDIC, stereo calibration with a cylinder of known radius is required while correcting for lens distortion with a checkerboard pattern is optional. An example of these calibration techniques is found in the Appendix.

2.3 Experimental Setup

The physical setup for data acquisition consists of a pair of high-speed cameras and lighting apparatus to obtain images for 3D-DIC analysis and the shaker table and laser displacement sensor to provide harmonic excitation at steady-state conditions, while also cross-checking the DIC results with the laser.

2.3.1 High-speed cameras and lighting setup

To measure the full-field dynamic response of the bistable beams, a pair of high-speed cameras (The Slow Motion Camera Company fps1000HD) and two LED lights (Neweer CN-216) must be setup facing the speckled surface of the beams and overhang. The cameras are mounted on separate Dolica Proline tripods to allow for adjusting of the height from the ground, angle of the lens, distance to the speckled surface, and angle between both cameras. The LED lights are secured on a dual mount, which is fastened onto an Amazon Basics tripod. Due to reflections from the lights that can lead to large error during DIC analysis, the lights are placed higher than the cameras and angled down toward the beams, avoiding the reflection of light from the speckled surface into the lens of the cameras. This setup is seen in Figure 7.

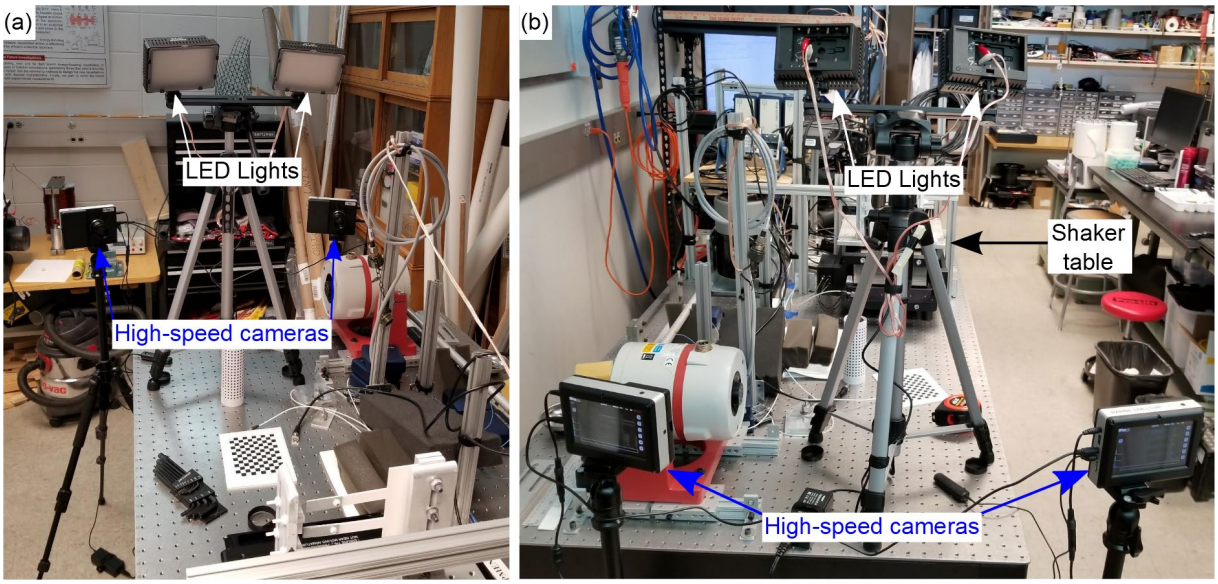

Figure 7: Setup of high-speed cameras and LED lights. (a) Front view of cameras and LED light sources directed toward speckled array of bistable beams mounted on electrodynamic shaker table; (b) Rear view of camera LCD screen interface, with voltage trigger and 2.5mm daisy chain for synchronous recording.

Each camera is setup at the same height and distance away from the speckled surface of the beams. A 2.5 mm cable runs between the cameras, acting as a daisy chain to synchronize the image capture of the cameras. A Progo camera trigger is then used to control the recording act of the reference camera. By

interacting with the LCD screen on each camera after a given recording, the frames are saved on a MicroSD card and then transferred to a computer for DIC evaluation.

2.3.2 Shaker table setup and measurement devices

The array of globally-coupled bistable beams is mounted on an electrodynamic shaker (APS 400), which is fixed on an optical isolation table (Newport Smart Table UT2). An accelerometer (PCB 333B40) is attached to the shaker to measure the input acceleration to the beams while a laser triangulation displacement sensor (Micro Epsilon ILD1420-25) measures the output displacement at the end of beam 2. These signals are fed into a signal conditioning box (PCB 482C05), which is connected to a National Instruments data acquisition system (NI PXIe-1073, NI PXI-6368). The accelerometer is used in a feedback loop for the controller (Vibration Research VR9500) to maintain constant acceleration of the shaker. A power amplifier (Behringer EP4000) provides the adequate power for the shaker to operate in the desired steady state conditions.

With the signal from the laser displacement sensor, a frequency sweep is performed to identify the resonant frequency of the system. Then, the beams are excited at the resonant frequency for various dynamic cases and images are taken for DIC analysis.

2.4 3D DIC Analysis on frames

The frames first must be converted from raw images into a readable file format for analysis. The raw images are opened in Adobe Photoshop for previewing and trimming the total number of frames to capture meaningful data. The images are saved with Photoshop into a TIFF file format to maintain image quality.

DIC analysis is performed with MultiDIC, as previously mentioned. First, a region of interest is drawn around the beams and overhang inside a MATLAB-based Ncorr GUI on the reference frame. Then important DIC parameters must be established and optimized for accuracy. One parameter, the subset size, refers to the discretization of a speckle pattern into smaller groups. The subset size is defined by the width in pixels of an area encompassing a group of speckles and each subset is tracked from one frame to the next. Selecting a size leads to a tradeoff. Too small, and the subset size does not capture a unique, randomized pattern that is distinguishable from other subsets. Too large, and the displacement approximation can be inaccurate [27]. The subset size for this research was chosen to be 16 pixels, which encompassed approximately 5 speckles across the width. The overall speckled surface is large compared to the speckle size, allowing for a smaller subset size to be chosen while also capturing an adequate number of speckles in each subset. The other important DIC parameter is the subset spacing, which refers to the distance between data points. This presents a tradeoff between data resolution and efficiency of processing time. For this research, a step size of 4 is used for higher data resolution. These parameters were used to produce sensible results for severe impulse cases, where the beam tip velocity competed against the frame rate of the high-speed cameras, which were considered to be adequate under less severe displacements at steady state conditions. These parameters are summarized in Table 1.

Table 1: Key DIC parameters for obtaining full-field displacements

Parameter	Value
Subset size [px]	16
Step size [px]	4
Reference Frame	First

Due to the harmonic excitations operating at steady state on the shaker table, the rigid body motion must be removed to compare the relative beam displacements. DIC analysis must be performed on a small region on the aluminum clamp surface, which is equivalent to the displacement of the shaker table. Then, by tracking the Y-coordinate position of a single point in the RBM region through each frame, the mean of the periodic curve is taken to ensure that displacements are referenced from the unstable region between both stable equilibria. The same procedure is applied to the beam structure at a single point in the middle of the overhang, closest to the clamped edge. Adjustments are made to the MultiDIC code to subtract out the average rigid body motion and re-calculate displacements to reference the position between each equilibria for each frame in time. The MATLAB code to extract out single points, which also results in the figures for the beam tip displacement, is provided in the Appendix.

3 RESULTS AND DISCUSSIONS

This research analyzes five unique dynamic cases at steady state conditions. The following sections detail the findings from the DIC results of the displacements of the globally-coupled bistable beams. For full-field results, the entire structure is shown in the left column in (a1-e1) and the overhang with small sections of each beam is shown in the right column in (a2-e2). Each row corresponds to the same frame in time to match the dynamic behavior between the entire structure and the overhang. Four cases occurred at an excitation frequency of 15 Hz. The fourth case was subjected to an excitation frequency of 19 Hz.

3.1 Case 1, Snap-through dynamics of all three bistable beams

Figure 8 displays the response for the first case. All three beams exhibit an in-phase, nearly synchronized snap-through with large displacement amplitudes. Beam 2 experiences the largest displacement amplitude, followed by beam 1 and then beam 3. This is the severest case in terms of beam velocity and displacement amplitude and is captured well by the DIC results, giving confidence for the subsequent DIC examinations involving smaller beam displacements and velocities.

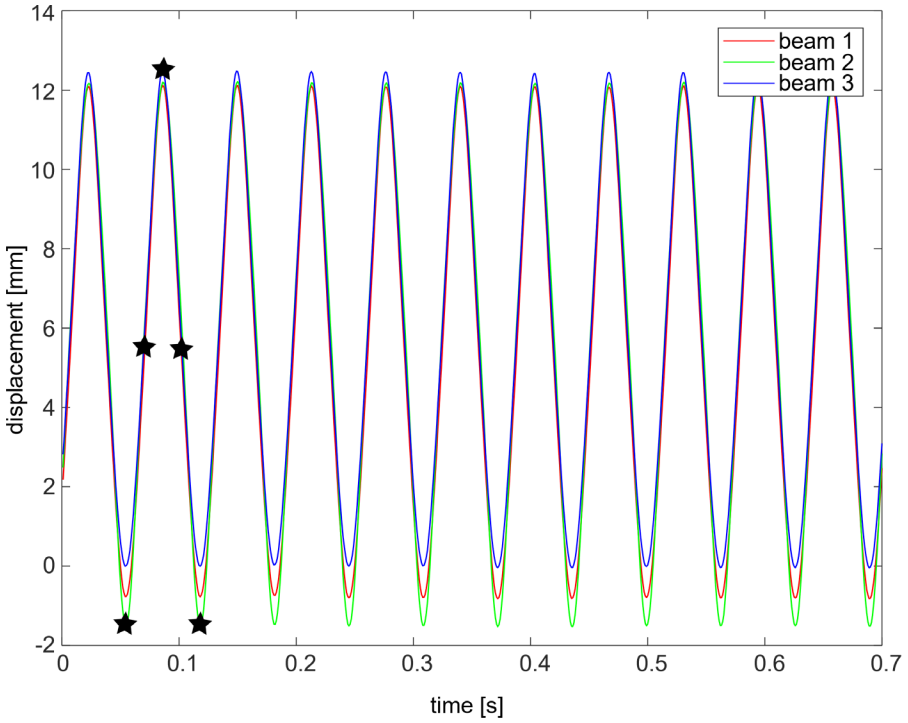

Figure 8: Time domain response of beam snap through dynamics measured experimentally with 3D DIC

Figure 9 (a1-e1) shows the corresponding full-field displacement results of the entire structure and Figure 9 (a2-e2) shows the full-field results for the overhang. Each frame in time is denoted by the black stars in Figure 8. As the five frames progress in time over one period, it is seen that the overhang consistently facilitates the snap-through dynamics for each bistable beams. This can be seen by the diminishing displacement magnitude toward the clamped end in the overhang from the local minimum at 0.055 s to the increase in magnitude to the local maximum at 0.087 s. A slight angle between the beams and the x-axis presents a distortion of the location of the unstable equilibrium. Since the surface of the beams is not parallel to the x-axis, the unstable equilibrium occurs at a nonzero value, seen in Figure 9 (b1, d1).

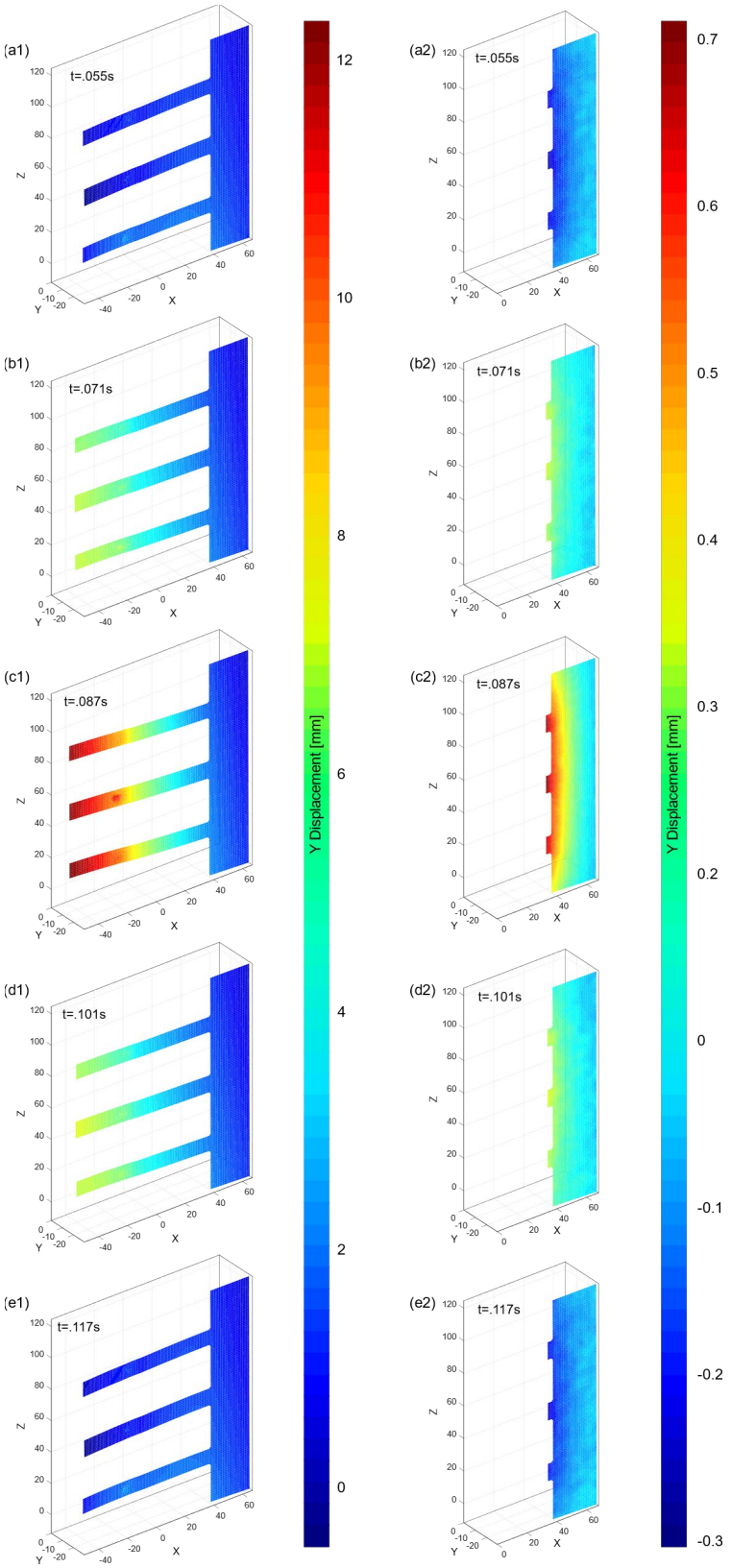

Figure 9: Case 1, all three beams snapping through. (a1-e1) Snapshots highlighting the displacement contour for the entire structure; (a2-e2) corresponding snapshots of the displacement contour throughout the overhang region.

3.2 Case 2, Intrawell dynamics of non-nearest neighbors

In this case, the beam tip displacement of beams 1 and 3 show large intrawell oscillations while beam 2 undergoes small amplitude intrawell, as seen in Figure 10. The non-nearest neighbors are oscillating in phase but not symmetrically about their stable equilibria. In fact, the overhang influences such asymmetric oscillations. This leads to one beam crossing into the unstable region where an overlap is seen between 5 and 6 mm of displacement. Then, the beam crosses back to toward its stable equilibrium while its non-nearest neighbor arrives at the unstable region. Beam 2 oscillates about its equilibrium at 2 mm and the other equilibrium is approximately 9mm, according to the measured global coupling parameters.

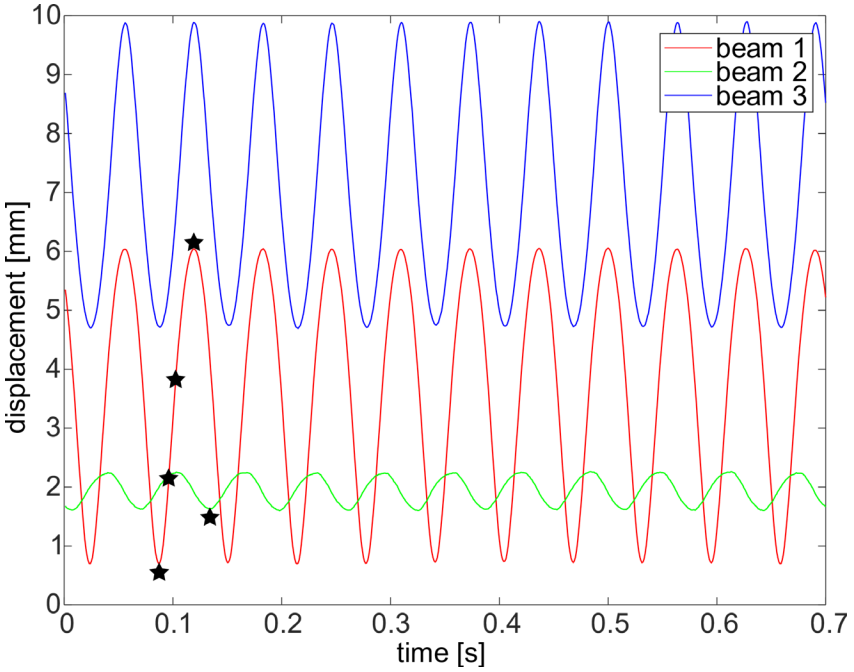

Figure 10: Time domain response of beam intrawell dynamics measured experimentally with 3D DIC

Figure 11 (a1-e1) shows the corresponding full-field displacement results of the entire structure and Figure 11 (a2-e2) shows the full-field results for the overhang. The black stars in Figure 10 correspond to each frame in time. The displacement amplitudes of beams 1 and 3 are seen to increase in time. Beam 3 is always at a higher relative displacement amplitude due to the position of its equilibrium with respect to the global coordinates. At 0.087 s, beams 1 and 3 are at local minima and transition to local maxima at 0.119 s. The overhang sees a diminishing magnitude of displacement around beams 1 and 3, and manages the in-phase, asymmetric intrawell oscillations of non-nearest neighbors. Depending on the parameters of the shared boundary between multistable structures, such as stiffness or damping, high amplitude snap-through may not be necessary for non-nearest neighbors to influence each other. Instead, smaller amplitude intrawell oscillations of one multistable structure can influence its non-nearest neighbors, which can easily transition into snap-through given enough input energy from an external mechanical load.

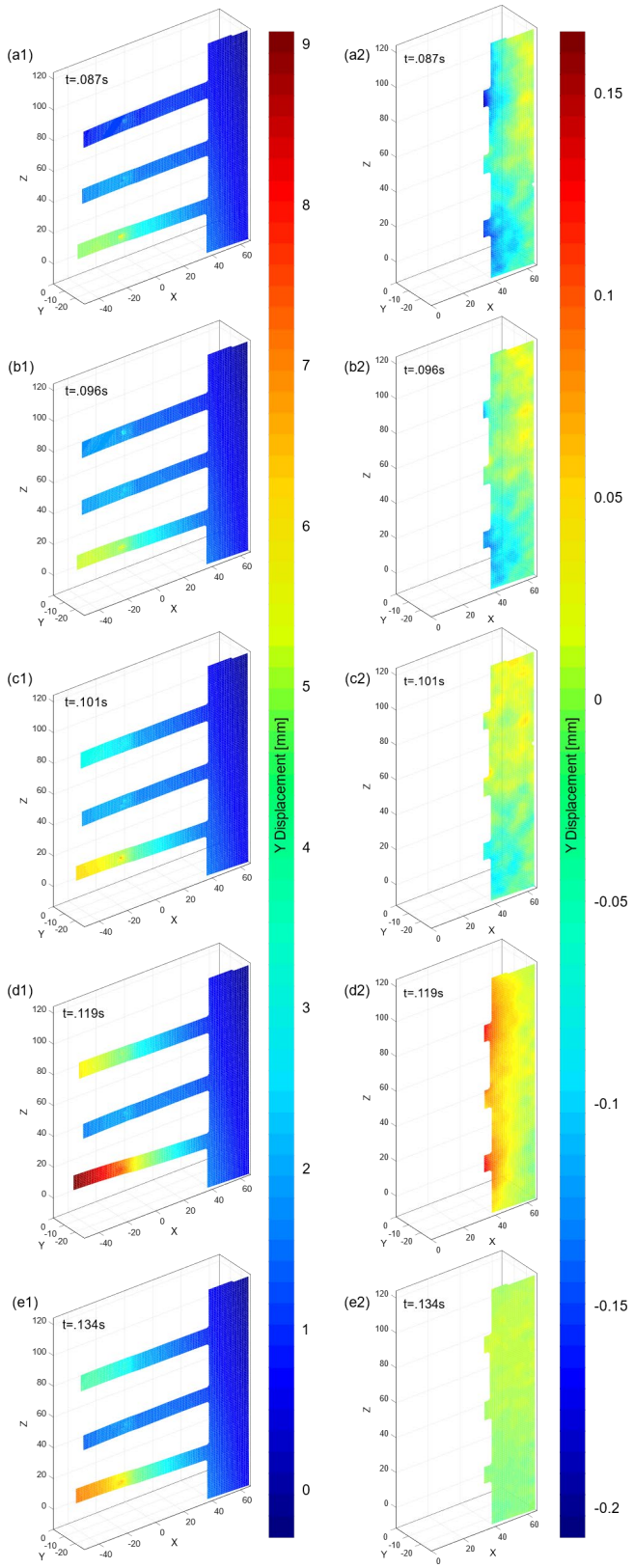

Figure 11: Case 2, large intrawell of beams 1 and 3. (a1-e1) Snapshots highlighting the displacement contour for the entire structure; (a2-e2) corresponding snapshots of the displacement contour throughout the overhang region.

3.3 Case 3, Snap-through and intrawell dynamics among neighboring beams

The third case displays the small amplitude intrawell response of beams 1 and 3 while beam 2 experiences suppressed snap-through, as seen in Figure 12. A phase lag exists between beam 2 and the other two beams, which are oscillating with each other in phase. As beam 2 reaches a local maximum, the other beams are moving toward their local minima. This local coupling interaction may explain why beam 2 experiences suppressed snap-through, and never reaches the stable equilibrium occurring around 9 mm.

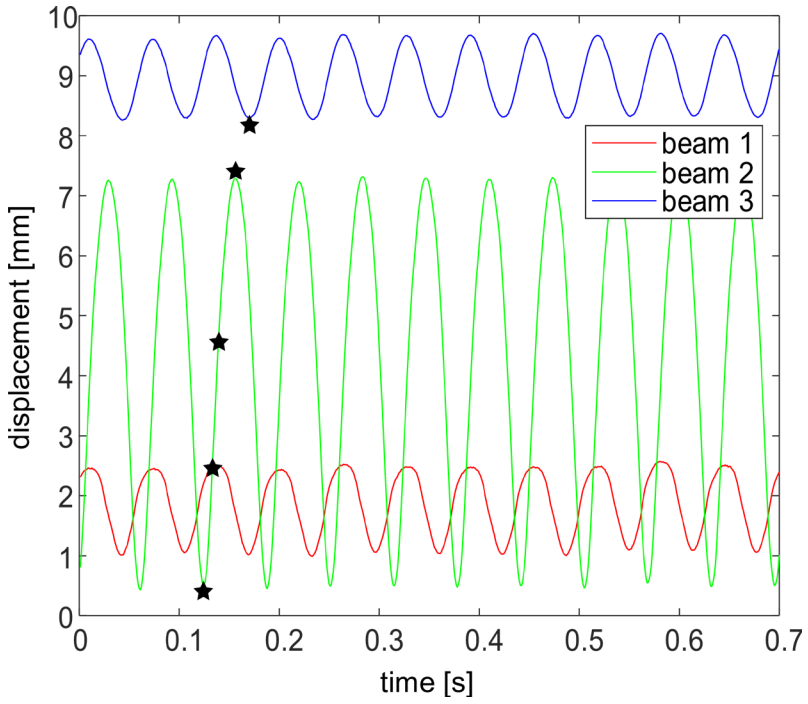

Figure 12: Time domain response of beam snap-through and intrawell dynamics measured experimentally with 3D DIC

Figure 13 (a1-e1) shows the corresponding full-field results of the entire structure and Figure 13 (a2-e2) shows the full-field results for the overhang. The displacement around beam 2 increases in magnitude and reaches its maximum at 0.156 s, also depicted by the fourth black star in Figure 12. The captured results with DIC on the overhang are consistent with the motion of beam 2 through time. Also, there is a bias towards the bottom of the overhang due to beam 3 always registering a higher displacement on the colorbar. Yet, the small amplitude intrawell of beams 1 and 3 do not provide enough amplitude through time to be seen with DIC.

In the rest of the overhang toward the clamped end, the subtraction of rigid body motion, consideration of oscillation about the unstable equilibrium, as well as the small change in displacements lead to the presence of noise, as indicated by the inconsistent colors. Additionally, the reprojection error after stereo calibration is about 0.04 mm. Yet, there is minimal impact on the overall dynamic behaviors presented in this case. This result is important for the implementation of 3D DIC to study multistable structures as various ranges of displacements may require optimization of different subset sizes.

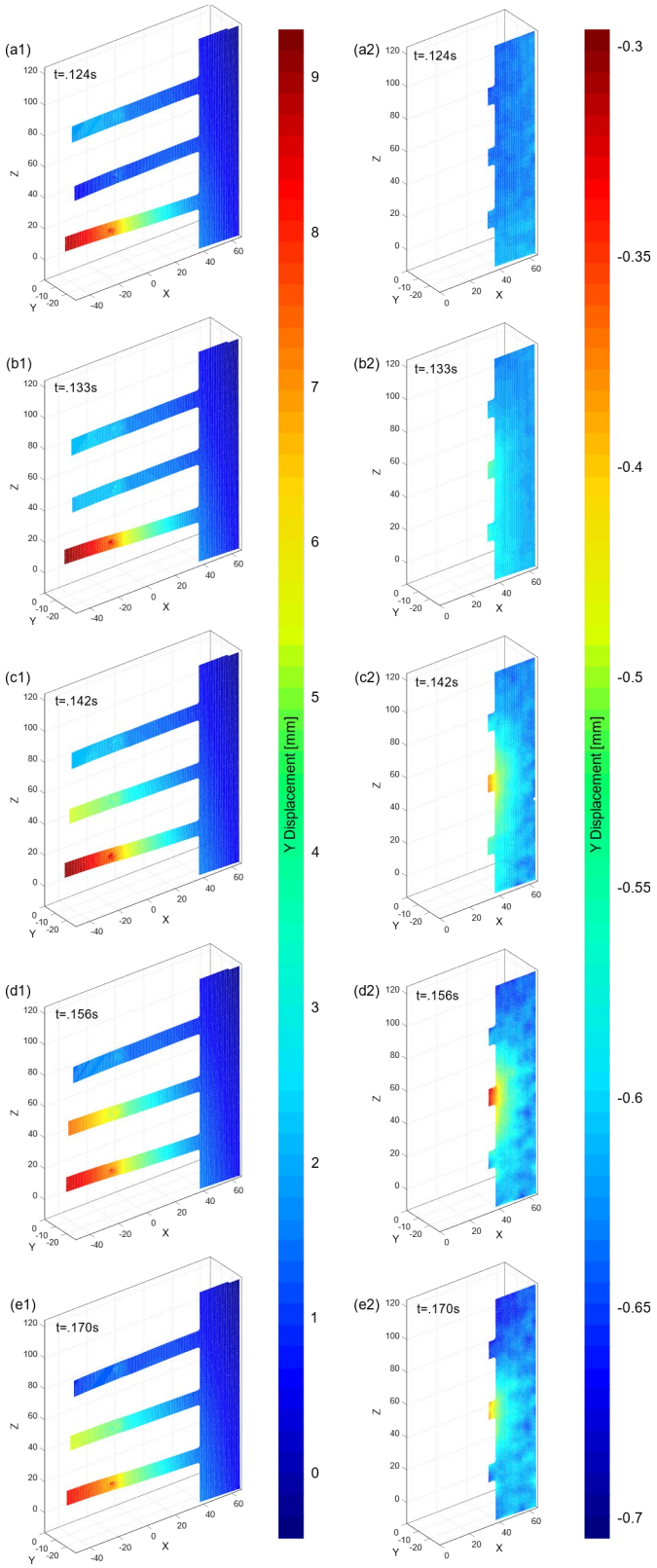

Figure 13: Case 3, suppressed snap-through of beam 2 and small intrawell for beams 1 and 3. (a1-e1) Snapshots highlighting the displacement contour for the entire structure; (a2-e2) corresponding snapshots of the displacement contour throughout the overhang region.

3.4 Case 4, Intrawell dynamics among all three bistable beams

The next case shows intrawell dynamics of equal amplitude, as seen in Figure 14. The beams were subjected to 19 Hz in this case as opposed to 15 Hz for the other cases. This was chosen from the softening trend occurring at the resonant frequency from the frequency sweep. All motion is in phase and beams 1 and 2 oscillate about one equilibrium while beam 3 oscillates about the other. Beams 1 and 3 do not switch to the other stable equilibrium during intrawell from one case to another. This could be due to imperfections in experiment, such as unequal volume of the steel inserts interacting with the magnets, possible plastic deformation of the acrylic, or stiffness from the white paint on one surface.

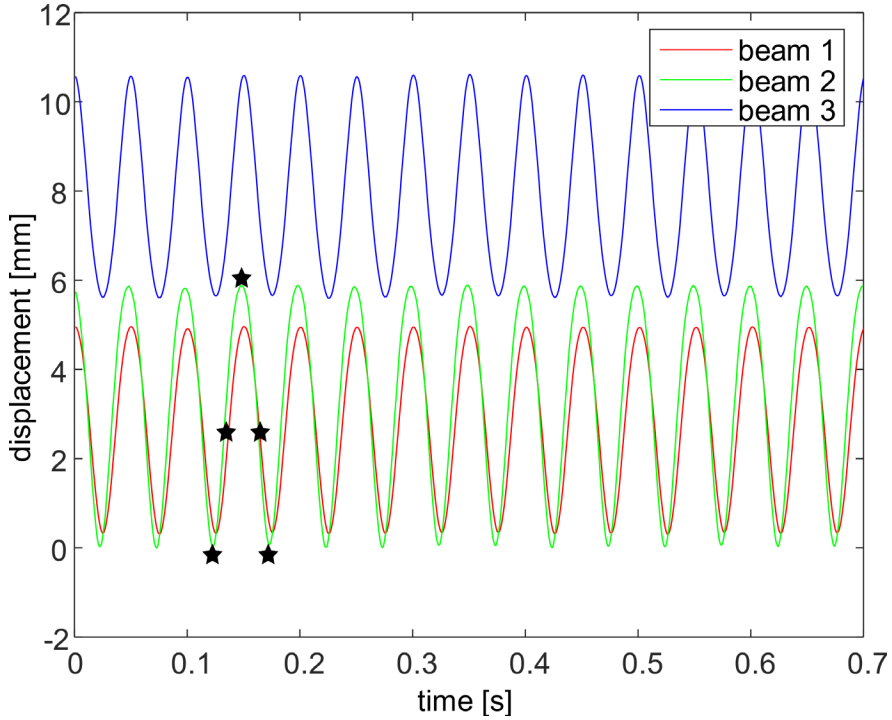

Figure 14: Time domain response of equal amplitude intrawell dynamics measured experimentally with 3D DIC

Figure 15 (a1-e1) shows the corresponding full-field displacement results of the entire structure and Figure 15 (a2-e2) shows the full-field results for the overhang. The black stars in Figure 14 correspond to each frame in time. The DIC captures the transition from local minima in amplitude at 0.123 s, to the local maxima at 0.148 s, and back to the local minima at 0.173 s. The progression in time is documented well for both the beams and the overhang. The displacement magnitude is seen to be diminishing in the overhang. The second and fourth frames in time are approximately zero displacement for the overhang to distinguish between the minimum and maximum displacement amplitudes.

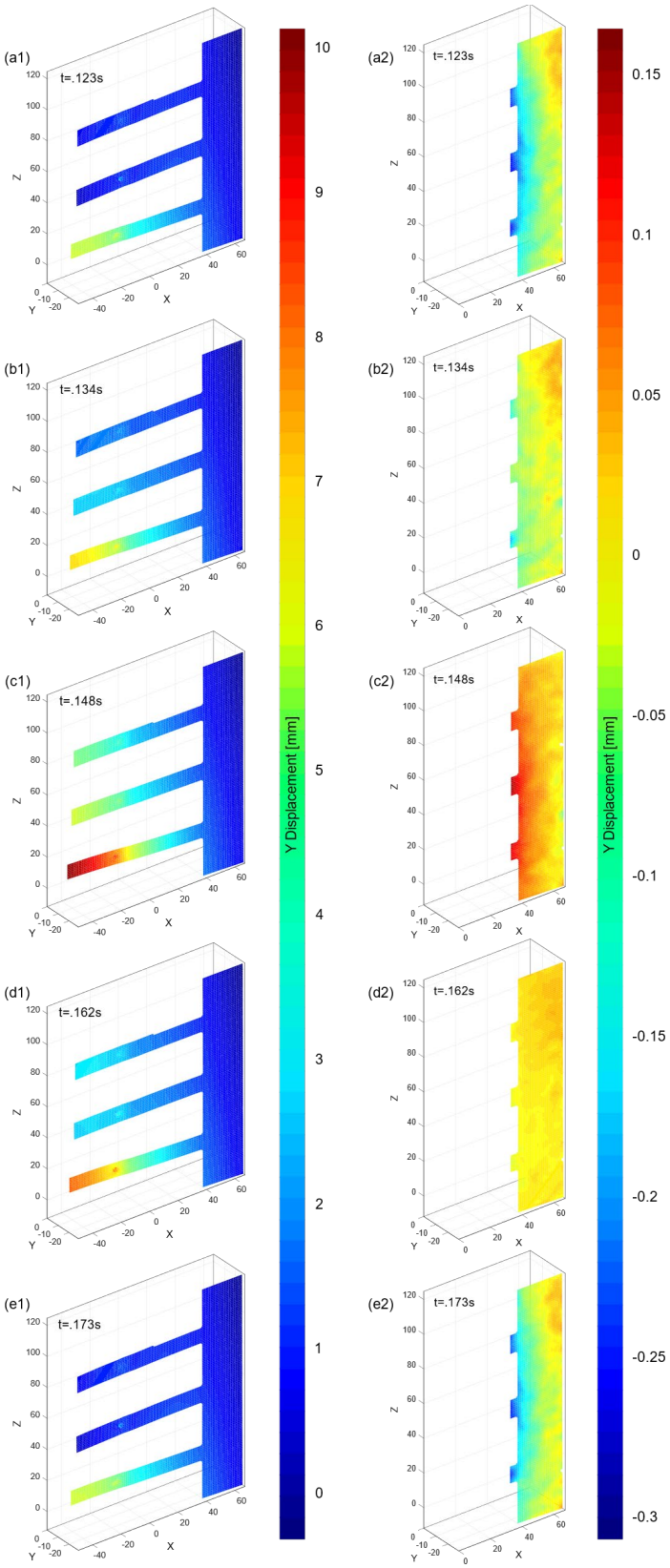

Figure 15: Case 4, equal amplitude intrawell for all three beams. (a1-e1) Snapshots highlighting the displacement contour for the entire structure; (a2-e2) corresponding snapshots of the displacement contour throughout the overhang region.

3.5 Case 4, Influence of snap-through dynamics between non-nearest neighbors

In the final case, as seen in Figure 16, beam 3 experiences large amplitude snap-through while the other beams encounter varying levels of intrawell displacement amplitude. A phase lag of approximately 90˚ from beam 3 to beam 1 may indicate a resistance of instantaneous energy exchange between the non-nearest neighbors. The combination of local and global coupling, as due to the phase lag and management by the overhang, leads to the varying levels of intrawell displacement amplitude of beam 1, which may also be on the verge of chaos.

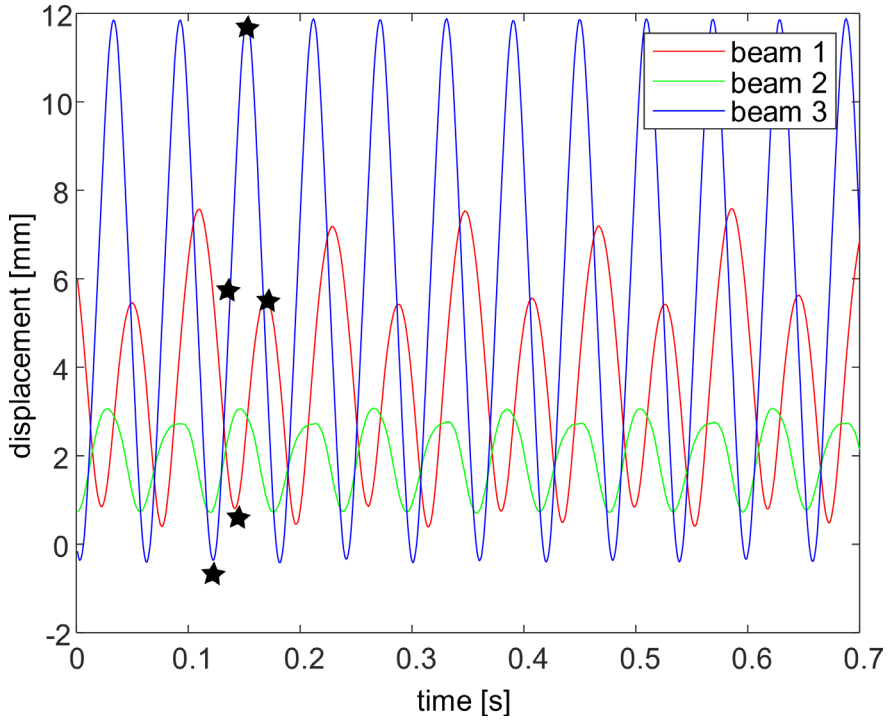

Figure 16: Time domain response of snap through and intrawell dynamics between non-nearest neighbors measured experimentally with 3D DIC

Figure 17 (a1-e1) shows the corresponding full-field results of the entire structure and Figure 17 (a2-e2) shows the full-field results for the overhang. The first four frames considered, as seen by black stars in Figure 16, progress in time and show the increase of displacement for beam 3. The overhang is seen bending in opposite directions for beams 1 and 3. The displacement magnitude at the interface of the overhang is drifting toward a minimum for beam 1 and a maximum for beam 3. The diminishing displacement around beam 3 also shows a bias towards beam 2 as the time sequence progresses from the second to the fourth point in time. The DIC results consistently capture the behavior of the beams and overhang

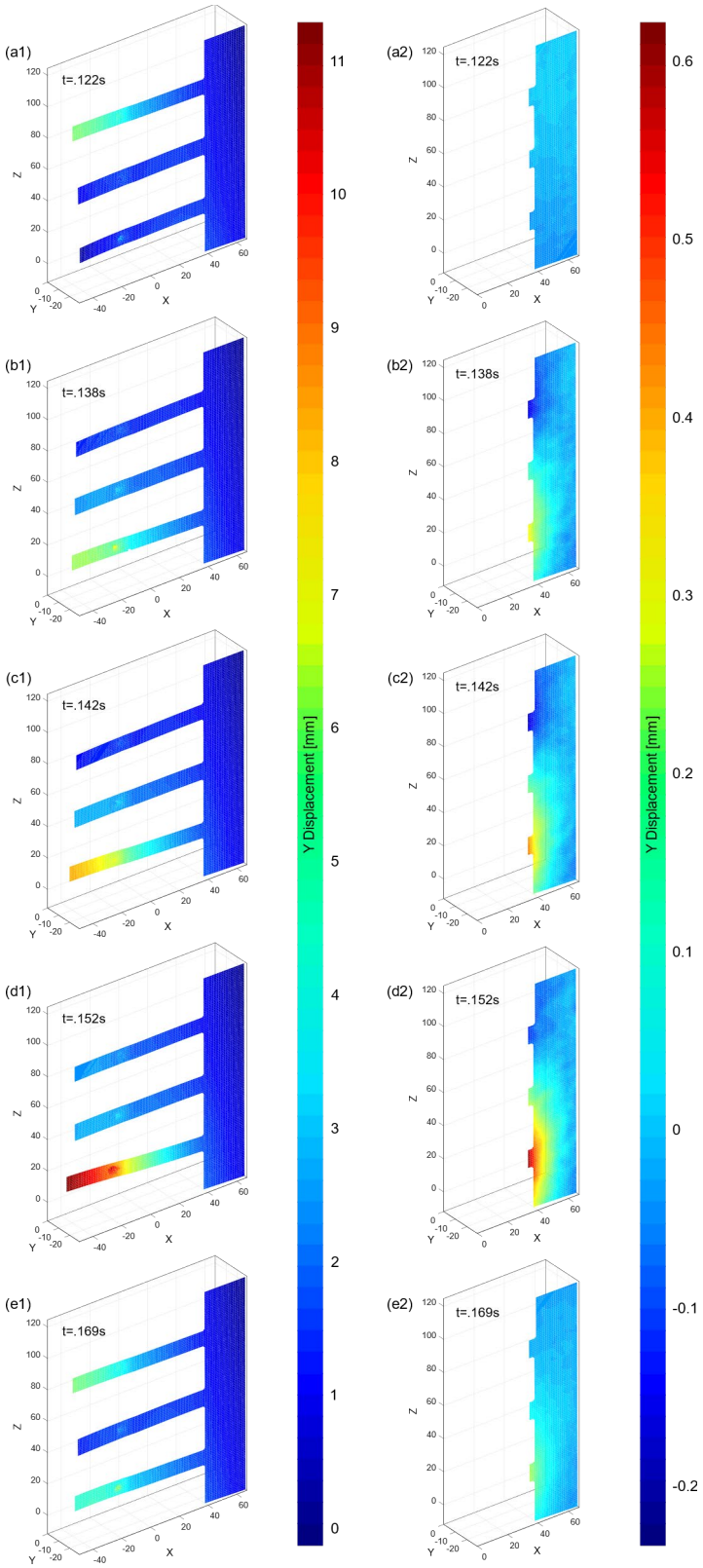

Figure 17: Case 5, snap-through and varying intrawell amplitude among non-nearest neighbors. (a1-e1) Snapshots highlighting the displacement contour for the entire structure; (a2-e2) corresponding snapshots of the displacement contour throughout the overhang region.

3.6 Observations of global coupling influences on dynamic behavior

The first case examines large-amplitude snap-through of all three bistable beams. The beams oscillate in phase, while driving the displacement in the overhang. As the beam tip displacements reach 12 mm in amplitude, the overhang is observed to reach 0.7 mm, nearly an order of magnitude difference. This case is analogous to the fundamental mode of the system, similarly seen in [12]. The even spacing between the beams along the overhang aids in maintaining the beams to be in phase with each other.

In the second case, non-nearest neighbors, depicted as beams 1 and 3, experience large amplitude intrawell, while oscillating in phase with one another. These beams cross the unstable region before crossing back to their respective stable equilibria, traveling 5 mm of displacement when transitioning from a local minimum to a local maximum. During this transition, the overhang experiences 0.35 mm in displacement magnitude, also an order of magnitude difference. Beam 2 experiences out-of-phase, small-amplitude intrawell and does not seem to have an impact on the dynamic behaviors of beams 1 and 3.

In the third case, beams 1 and 3 undergo intrawell oscillations with small amplitudes. At the same time, beam 2 experiences suppressed snap-through, traveling past the stable equilibrium of beam 1 without reaching the equilibrium of beam 3. From local minima to maxima, beam 2 travels about 7 mm, beams 1 and 3 travel between 1 mm and 1.5 mm, and the overhang displacements travel 0.4 mm. With only beam 2 driving the response of the other two beams, the difference in displacement amplitude between the overhang and beams 1 and 3 is less than an order of magnitude. This result shows that the overhang enables the phase lag, and thus a combination of local and global coupling could be the source of the suppressed snap-through of beam 2.

Next, the fourth case displays similar amplitude intrawell oscillations of all three beams. Beams 1 and 2 oscillate about one equilibrium and beam 3 oscillates about the other, with all motion in phase. The overhang is driven by the in-phase oscillation of the three beams, with the beam tip displacements reaching between 5 and 6 mm from minima to maxima, while the overhang sees about 0.45 mm from minima to maxima.

Finally, the fifth case analyzes the influence that snap-through of one bistable beam has on a non-nearest neighbor. Similar to the third case where only one beam experiences the largest displacement amplitude, a phase lag is produced. The overhang is seen to displace 0.8 mm while beam 2 is seen to displace 2 mm, from minima to maxima. Again, a similar order of magnitude of these displacements is observed, which shows that the overhang is able to influence the phase lag and small varying levels of displacement in beam 2. Though larger, varying levels of intrawell displacement amplitude are also seen in beam 1, likely due to the combination of local and global coupling. Beam 1 varies from 4 mm to 6 mm of displacement between minima and maxima, every other oscillation. This large variation makes the beam more prone to snap-through and possibly chaos.

Whether the dynamics are characterized by snap-through, intrawell, or phase lags, these unique cases demonstrate that global coupling is able to influence the dynamic behavior between multistable structures.

4 CONCLUSIONS

Multistable structures are manifest in a wide variety of applications. For energy harvesters, they can be used to enhance performance. Slender structural components can experience large amplitude dynamics due multistability. For the skin panels on hypersonic aircraft, the skin buckling can lead to fatigue and eventual structural failure. Because of their susceptibility to failure in real world applications, it is important to understand the dynamic interactions among coupled multistable structures. With advanced methods, researchers continue to expand upon the current understanding of multistable structures to better predict the undesirable dynamic behaviors of built-up structures.

This research establishes 3D DIC as an experimental method to investigate the roles of global coupling on an archetypal multistable structure. The trio of cantilevered beams joined together with a shared boundary and subjected to a bistable configuration with the use of permanent attractive magnets is a simplified representation of complex skin panels. The full-field displacements from DIC can be used to gain insights into the dynamic behaviors occurring at the shared boundary between the bistable beams.

It is found that DIC can accurately measure the out-of-plane displacements of a multistable structure subjected to harmonic excitations at steady state conditions. This is accomplished at a relatively low cost, without commercial software packages or products. It is seen that the overhang effectively facilitates the energy transfer and thus influences the displacement magnitudes between nearest and non-nearest neighbors. In the first case, large amplitude intrawell responses can influence the behavior between multistable structures due to the interaction through a shared boundary. This can cause bistable beams to cross an unstable region without reaching the other stable equilibrium. Also, global coupling can lead to a phase lag between neighboring multistable structures and thus a resistance to an instantaneous exchange of energy. In the last case, snap-through of one bistable beam is seen to influence the varying levels of displacement amplitude during the intrawell response of a non-nearest neighbor.

Future investigations should consider metallic materials, which are not as susceptible to plastic deformation as acrylic and have little mechanical damping. This would eliminate the use of steel inserts that can cause uneven attractive forces to one magnet over another. It would also reveal the higher-order harmonics that can be present in the system. Also, various overhang lengths should be considered to further verify the influences of global coupling on the dynamic responses.

5 BIBLIOGRAPHY

[1] R. D. Blevins, I. Holehouse and K. R. Wentz, "Thermoacoustic loads and fatigue of hypersonic vehicle skin panels," *Journal of Aircraft,* vol. 30, no. 6, pp. 971-978, 1993.

[2] D. Quinn, A. Murphy and L. Cervi, "Fatigue performance of aircraft panels with novel skin buckling containment features," *Journal of Aerospace Engineering,* vol. 225, pp. 791-806, 2011.

[3] G. Houston, D. Quinn, A. Murphy and F. Bron, "Wing Panel Design with Novel Skin-Buckling Containment Features," *Journal of Aircraft,* vol. 53, no. 2, pp. 416-426, 2016.

[4] R. L. Harne and B. A. Goodpaster, "Impedance measures in analysis and characterization of multistable structures subject to harmonic excitation," *Mechanical Systems and Signal Processing,* vol. 98, pp. 78-90, 2018.

[5] M. Conner, "SR-71 Image Gallery," NASA, 3 August 2017. [Online]. Available: https://www.nasa.gov/centers/armstrong/multimedia/imagegallery/SR-71/index.html. [Accessed 17 January 2019].

[6] Boeing, "B-52," [Online]. Available: http://www.boeing.com/defense/b-52-bomber.

[7] G. Arena, R. M. J. Groh, A. Brinkmeyer, R. Theunissen, P. M. Weaver and A. Pirrera, "Adaptive compliant structures for flow regulation," *The Royal Society Publishing,* vol. 473, no. 2204, 2017.

[8] R. Harne and K. Wang, Harnessing Bistable Structural Dynamics: for Vibration Control, Energy Harvesting and Sensing, Chichester: John Wiley & Sons Ltd., 2017.

[9] R. Wiebe, L. N. Virgin, I. Stanciulescu, S. M. Spottswood and T. G. Eason, "Characterizing Dynamic Transitions Associated With Snap-Through: A Discrete System," *Journal of Computational and Nonlinear Dynamics,* vol. 8, no. 1, p. 11010, 2012.

[10] S. Spottswood, T. Eason and R. Chona, "A structural perspective on the challenges associated with analyzing a reusable hypersonic platform," in *Proceedings of the 11th International Conference on Recent Advancements on Structural Dynamics*, Pisa, Italy, 2013.

[11] S. Sridharan and M. Peng, "Performance of Axially Compressed Stiffened Panels," *International Journal of Solids and Structures,* vol. 25, no. 8, pp. 879-899, 1989.

[12] D. F. Wang, T. Chatani, K. Ikelhara and R. Maeda, "Observation of localised vibration modes in a micromechanical oscillator trio with coupling overhang for highly sensitive mass sensing," *Micro & Nano Letters,* vol. 7, no. 8, pp. 713-716, 2012.

[13] H. Pakdast and M. Lazzarino, "Triple coupled cantilever systems for mass detection and localization," *Sensors and Actuators: A Physical ,* vol. 175, pp. 127-131, 2012.

[14] M. Sato, B. E. Hubbard and A. J. Sievers, "Colloquium: Nonlinear energy localization and its manipulation in micromechanical oscillator arrays," *Reviews of Modern Physics,* vol. 78, pp. 137-157, 2006.

[15] D. F. Wang, X. Li, X. Yang, T. Ikehara and R. Maeda, "Enhancing amplitude changes by mode localization in tro cantilevers with mass perturbation," *Journal of Micromechanics and Microengineering,* vol. 25, no. 9, p. 095017, 2015.

[16] E. Gil-Santos, D. Ramos, V. Pini, M. Calleja and J. Tamayo, "Exponential tuning of the coupling constant of coupled microcantilevers by modifying their separation," *Applied Physics Letters,* vol. 98, p. 123108, 2011.

[17] B. A. Goodpaster and R. L. Harne, "Modal evaluation and generalized analysis of the steady-state dynamics of harmonically excited multistable structures," *Journal of Sound and Vibration,* vol. 432, pp. 387-404, 2018.

[18] R. Wiebe and S. Spottswood, "On the dimension of complex responses in nonlinear structural vibrations," *Journal of Sound and Vibration,* vol. 373, pp. 192-204, 2016.

[19] B. A. Goodpaster and R. L. Harne, "Analytical modeling and impedance characterization of the nonlinear dynamics of thermomechanically coupled structures," *Journal of Applied Mechanics,* vol. 85, p. 081010, 2018.

[20] B. Miller, J. McNamara, S. Spottswood and A. Culler, "The impact of flow induced loads on snap-through behavior of acoustically excited, thermally buckled panels," *Journal of Sound and Vibration,* vol. 330, pp. 5736-5752, 2011.

[21] P. Reu, "The Art and Application of DIC," *Experimental Techniques ,* 2012.

[22] L. Virgin, "The dynamics of symmetric post-buckling," *International Journal of Mechanical Sciences,* vol. 27, pp. 235-248, 1985.

[23] Q. Dai and R. L. Harne, "Investigation of direct current power delivery from nonlinear vibration energy harvesters under combined harmonic and stochastic excitations," *Journal of Intelligent Material Systems and Structures,* vol. 29, pp. 514-529, 2017.

[24] F. Moon and P. Holmes, "A magnetoelastic strange attractor," *Journal of Sound and Vibration,* vol. 65, pp. 275-296, 1979.

[25] E. Byrne and N. Lovaas, "Speckle pattern fundamentals," 19 February 2018. [Online]. Available: http://www.correlatedsolutions.com/support/index.php?/Knowledgebase/Article/View/80/0/speckle-pattern-fundamentals. [Accessed 28 November 2018].

[26] D. Solav, K. M. Moerman, A. M. Jaegar, K. Genovese and H. M. Herr, "MultiDIC: an open-source toolbox for multi-view 3D digital image correlation," *IEEE Access,* vol. 6, pp. 30520-30535, 2018.

[27] B. Pan, H. Xie, Z. Wang, K. Qian and Z. Wang, "Study on subset size selection in digital image correlation for speckle patterns," *Optical Society of America,* vol. 16, no. 10, pp. 7037-7048, 2008.

6 APPENDIX

6.1 Sample calibration patterns for 3D DIC analysis utilizing MultiDIC

Figure 18 shows the calibration patterns used in this research.

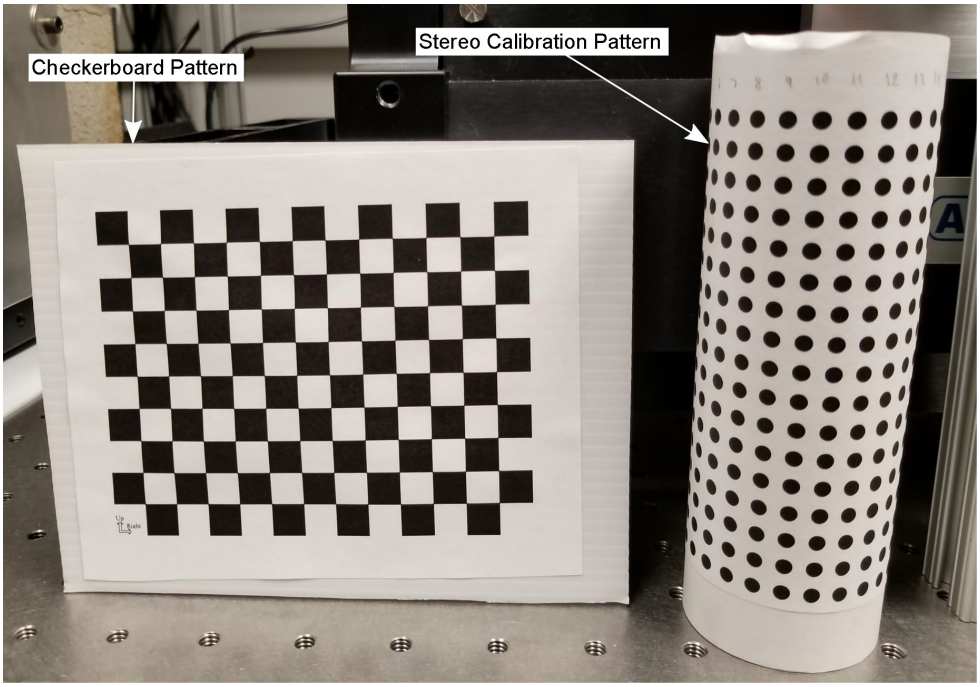

Figure 18: Both calibration patterns

6.2 Sample MATLAB Code to obtain single displacement points from MultiDIC

```
%% Obtain Single Displacement Point
%Load post-processed data from Step 4 results. Use file location of
%DIC3DPPresults_#Pairs results structure
d = load('C:\Users\denise.4\Documents\MultiDIC-
master\Experiments\2019_02_28_Globally_coupled_array_steady_state\D08 -
DIC_middle_bottom_large_intrawell_19Hz\ARBM Equil Post
Processed\DIC3DPPresults_1Pairs.mat');
RBM = load('C:\Users\denise.4\Documents\MultiDIC-
master\Experiments\2019_02_28_Globally_coupled_array_steady_state\D08 -
DIC_middle_bottom_large_intrawell_19Hz\RBM Region\Post Processed
Equil\DIC3DPPresults_1Pairs.mat');
RBM_Disp_Vec = RBM.DIC3DPPresults.Disp.DispVec;
RBM_points3D = RBM.DIC3DPPresults.Points3D;
%Create new variables for relevant cells
points3D=d.DIC3DPPresults.Points3D;
num_Frames=length(points3D);
num_rows = size(points3D{1}, 1);
Disp_vector = d.DIC3DPPresults.Disp.DispVec;
Disp_mgn = d.DIC3DPPresults.Disp.DispMgn;
for iii = 1:length(RBM_Disp_Vec)
  RBM_Avg_Disp_Y(iii) = nanmean(RBM_Disp_Vec{iii}(:,2));
  RBM_Avg_Points_Y(iii) = nanmean(RBM_points3D{iii}(:,2));
end
```

```
%% Choose the range and position for the top beam [Beam 1]
%Pattern of filling out matrix of 3D points reveals x and z range for end
%of the top beam
%Use find to extract the indices that match the generous range criteria
for i=1:length(points3D)
  range_top{i} = find(points3D{i}(:,3)>88 & points3D{i}(:,1)<-48); %higher
than 88mm in z, lower than -48mm in x
end
%Find the length of each cell (frame) that meets the range criteria
length_cells_top = cellfun('length',range_top);
length_cells_top(length_cells_top==0)=inf;
%Due to the generous range, the longer cells include points that are not
%quite at the end of the beam. Take the smallest cell.
[val_top,index_top]=min(length_cells_top);
%Extract the rows that have points at the end of the beam
new_range_top = range_top{index_top};
%Take the middle of the new range. This is the index used to get
%displacement at the end of the beam.
midrow_top = new_range_top(ceil(end/2));
%% Choose the range and position for the middle beam [Beam 2]
%Similar procedure for the top beam. This time, the range of 3D points have
%to be narrowed further with intersect
for ii=1:length(points3D)
    range_middle_condition_z{ii}=find(points3D{ii}(:,3)> 50 &
points3D{ii}(:,3)<60); %between 50 and 60mm in z
    range_middle_condition_x{ii}=find(points3D{ii}(:,1)<-49); %lower than 49
mm in x
    range_middle{ii}=num2cell(intersect(range_middle_condition_z{ii},
range_middle_condition_x{ii}));
end
%Find length of each cell (frame) that fits the criteria
length_cells_middle = cellfun('length',range_middle);
%If no intersection between the x and z ranges, the length of the cell
%array is 0. Force the length to be inf.
length_cells_middle(length_cells_middle==0)=inf;
%Take the smallest cell.
[val_middle,index_middle]=min(length_cells_middle);
%Extract the rows that have points at the end of the beam
new_range_middle = range_middle{index_middle};
%Take the middle of the new range, use as index for displacement
midrow_middle = cell2mat(new_range_middle(ceil(end/2)));
%% Choose the range and position for the bottom beam [Beam 3]
%Exact procedure for the top beam. 3D points are in different ranges.
for i=1:length(points3D)
  range_bottom{i} = find(points3D{i}(:,3)<22 & points3D{i}(:,1)<-49); %lower
than 22mm in z. Lower than 49mm in x
end
length_cells_bottom = cellfun('length',range_bottom);
length_cells_bottom(length_cells_bottom==0)=inf;
[val_bottom,index_bottom]=min(length_cells_bottom);
new_range_bottom = range_bottom{index_bottom};
midrow_bottom = new_range_bottom(ceil(end/2));
%% Create displacement vectors and plot the results
%Create column vector of displacement at the end of each beam, in the
%middle. Each row represents a new frame in time (1000 fps)
%**The 3D coordinate in the y direction of the overhang near aluminum
```

```
%clamps was chosen as the equilbrium point to compute alternative
%displacements instead of referencing the first frame.
for k=1:length(Disp_vector)
  y_disp_top(k,1) = Disp_vector{k}(midrow_top,2);
  y_disp_middle(k,1) = Disp_vector{k}(midrow_middle,2);
  y_disp_bottom(k,1) = Disp_vector{k}(midrow_bottom,2);

  y_disp_top_equil(k,1) = points3D{k}(midrow_top,2)-(RBM_Avg_Disp_Y(k))-(-
27.465); %check that displacements were calculated correctly
  y_disp_middle_equil(k,1) = points3D{k}(midrow_middle,2)-
(RBM_Avg_Disp_Y(k))-(-27.465);
  y_disp_bottom_equil(k,1) = points3D{k}(midrow_bottom,2)-
(RBM_Avg_Disp_Y(k))-(-27.465);

  y_disp_test(k,1) = Disp_vector{k}(64,2); %check RBM of overhang, to make
sure that it is approximately zero
 end
%Plot the results
time = [0.001:0.001:0.700];
clf;
figure(1)
plot(time,y_disp_top,'-r',time,y_disp_middle,'-g',time,y_disp_bottom,'-b')
xlabel('time[s]')
ylabel('displacement[mm]')
legend('beam 1','beam 2','beam 3','location','northeast')
figure(2)
plot(time,y_disp_top_equil,'-r',time,y_disp_middle_equil,'-
g',time,y_disp_bottom_equil,'-b')
xlabel('time[s]')
ylabel('displacement[mm]')
legend('beam 1','beam 2','beam 3','location','northeast')
title('About Equilibrium')
figure(3)
plot(time,y_disp_test,'-ro')
legend('Points at overhang','location','northeast')
xlabel('time[s]')
ylabel('displacement[mm]')
```

6.3 Sample MATLAB code used to post process the DIC results and plot

In this code, the rigid body motion of the shaker table is removed while also calculating displacement with respect the y-coordinate of the unstable region.

```
%% STEP 4: Post Processing
% Upload 3D reconstructed points (either as seperate pairs or a stitched
surface)
% and calculate diplacements, deformations, and strains.

%%
clearvars; close all

fs=get(0, 'DefaultUIControlFontSize');
set(0, 'DefaultUIControlFontSize', 10);

%% Load Rigid Body Motion Results
```

```
RBM = load('C:\Users\denise.4\Documents\MultiDIC-
master\Experiments\2019_02_28_Globally_coupled_array_steady_state\D08 -
DIC_middle_bottom_large_intrawell_19Hz\RBM Region\Post Processed - Frame
11\DIC3DPPresults_1Pairs.mat');
RBM_Disp_Vec = RBM.DIC3DPPresults.Disp.DispVec;

for iii = 1:length(RBM_Disp_Vec)
    RBM_Avg_Disp_Y(iii) = nanmean(RBM_Disp_Vec{iii}(:,2)); %Obtain the mean
y-displacement of the rigid body motion for each frame
end
%% CHOOSE PATHS OPTIONS

% select DIC3DpairResults structures
PathInitial=pwd;
[file,path] = uigetfile(PathInitial,'Select a 3D-DIC results structure
(stitched or unstitched)');

DIC3D=load([path file]);
DIC3Dname=fieldnames(DIC3D);
DIC3D=DIC3D.(DIC3Dname{1});

% save 3D-DIC post processing results? choose save path and overwrite options
[save3DDIClogic,savePath]=Qsave3DDICPPresults(path);


%% 3D reconstruction using Direct Linear Transformation

nImages= numel(DIC3D.Points3D);

% pre-allocate 3D-DIC result variables
DIC3D.Points3D_ARBM=cell(1,nImages);
DIC3D.Disp.DispVec=cell(1,nImages);
DIC3D.Disp.DispMgn=cell(1,nImages);
DIC3D.Disp.DispVec_ARBM=cell(1,nImages);
DIC3D.Disp.DispMgn_ARBM=cell(1,nImages);
DIC3D.FaceCentroids=cell(1,nImages);
DIC3D.FaceCentroids_ARBM=cell(1,nImages);
DIC3D.FaceCorrComb=cell(1,nImages);
DIC3D.FaceIsoInd=cell(1,nImages);
DIC3D.RBM.RotMat=cell(1,nImages);
DIC3D.RBM.TransVec=cell(1,nImages);

F=DIC3D.Faces;

hw = waitbar(0,'Calculating displacements and rigid body motion');
for ii=1:nImages % loop over images (time frames)
    waitbar(ii/(nImages));

    % Face correlation coefficient (worst)
    DIC3D.FaceCorrComb{ii}=max(DIC3D.corrComb{ii}(F),[],2);

    % compute face centroids
    for iface=1:size(F,1)

DIC3D.FaceCentroids{ii}(iface,:)=mean(DIC3D.Points3D{ii}(F(iface,:),:));
    end
```

```
    % Compute displacements between frames (per point)
    %Subtract from equilibrium after obtaining equil point
%   DispVec=DIC3D.Points3D{ii}-DIC3D.Points3D{1}; %References the first
%   frame
    DispVec=DIC3D.Points3D{ii}-(-21.6616); %Oscillation about unstable region
    DIC3D.Disp.DispVec{ii}=DispVec;

    %Remove rigid body motion
    DIC3D.Disp.DispVec{1,ii}(:,2)=DIC3D.Disp.DispVec{1,ii}(:,2)-
RBM_Avg_Disp_Y(ii);


DIC3D.Disp.DispMgn{ii}=sqrt(DispVec(:,1).^2+DispVec(:,2).^2+DispVec(:,3).^2);


    % Compute rigid body transformation between point clouds

[RotMat,TransVec,Points3D_ARBM]=rigidTransformation(DIC3D.Points3D{ii},DIC3D.
Points3D{1});
    DIC3D.RBM.RotMat{ii}=RotMat;
    DIC3D.RBM.TransVec{ii}=TransVec;
    DIC3D.Points3D_ARBM{ii}=Points3D_ARBM;

    % Compute displacements between sets - after RBM
    DispVec=DIC3D.Points3D_ARBM{ii}-DIC3D.Points3D_ARBM{1};
    DIC3D.Disp.DispVec_ARBM{ii}=DispVec;

DIC3D.Disp.DispMgn_ARBM{ii}=sqrt(DispVec(:,1).^2+DispVec(:,2).^2+DispVec(:,3)
.^2);

    % compute face centroids - after transformation
    for iface=1:size(F,1)

DIC3D.FaceCentroids_ARBM{ii}(iface,:)=mean(Points3D_ARBM(F(iface,:),:));
    end

end
delete(hw);


% % compute deformation and strains (per triangular face)
%
deformationStruct=triSurfaceDeformation(F,DIC3D.Points3D{1},DIC3D.Points3D);
% DIC3D.Deform=deformationStruct;
%
%
deformationStruct_ARBM=triSurfaceDeformation(F,DIC3D.Points3D_ARBM{1},DIC3D.P
oints3D_ARBM);
% DIC3D.Deform_ARBM=deformationStruct_ARBM;
%
% % compute triangle regularity (isotropy index)
% for ii=1:nImages
%     [FisoInd]=faceIsotropyIndex(F,DIC3D.Points3D{ii});
%     DIC3D.FaceIsoInd{ii}=FisoInd;
% end

DIC3DPPresults=DIC3D;
```

```
%% save results
nPairs=size(DIC3DPPresults.pairIndices,1);
if save3DDIClogic
    saveName=fullfile(savePath, ['DIC3DPPresults_' num2str(nPairs)
'Pairs.mat']);
    icount=1;
    while exist(saveName,'file')
        saveName=fullfile(savePath, ['DIC3DPPresults_' num2str(nPairs)
'Pairs(' num2str(icount) ').mat']);
        icount=icount+1;
    end
    save(saveName,'DIC3DPPresults','-v7.3');
end

%% Plot results?

plotButton = questdlg('Plot 3D-DIC post-processing results?', 'Plot?', 'Yes',
'No', 'Yes');
switch plotButton
    case 'Yes'
        plotMoreLogic=true;
        while plotMoreLogic
            optStruct=struct;
            optStruct.zDirection=1;
            optStruct.FaceAlpha=1;
            optStruct.smoothLogic=1;
            % PLOT
            plot3DDICPPresults(DIC3DPPresults,optStruct);

            plotMoreButton = questdlg('Plot more results?', 'Plot?', 'Yes',
'No', 'Yes');
            switch plotMoreButton
                case 'Yes'
                    plotMoreLogic=true;
                case 'No'
                    plotMoreLogic=false;
            end
        end
    case 'No'
end

%% finish
h=msgbox('STEP4 is completed');
h.CurrentAxes.Children.FontSize=11;

set(0, 'DefaultUIControlFontSize', fs);

%%
% MultiDIC: a MATLAB Toolbox for Multi-View 3D Digital Image Correlation
%
% License: <https://github.com/MultiDIC/MultiDIC/blob/master/LICENSE.txt>
%
% Copyright (C) 2018  Dana Solav
%
% If you use the toolbox/function for your research, please cite our paper:
```

% <https://engrxiv.org/fv47e>